

UNIVERSITY OF BIRMINGHAM

Research at Birmingham

Dislocation network in additive manufactured steel breaks strength–ductility trade-off

Liu, Leifeng; Zhong, Yuan; Zou, Ji; Wu, Jing; Chiu, Yu-Lung; Shen, James Zhijian

DOI:

[10.1016/j.mattod.2017.11.004](https://doi.org/10.1016/j.mattod.2017.11.004)

License:

Creative Commons: Attribution-NonCommercial-NoDerivs (CC BY-NC-ND)

Document Version

Peer reviewed version

Citation for published version (Harvard):

Liu, L, Zhong, Y, Zou, J, Wu, J, Chiu, Y-L & Shen, JZ 2017, 'Dislocation network in additive manufactured steel breaks strength–ductility trade-off', *Materials Today*. <https://doi.org/10.1016/j.mattod.2017.11.004>

[Link to publication on Research at Birmingham portal](#)

Publisher Rights Statement:

Checked for eligibility: 22/12/2017

General rights

Unless a licence is specified above, all rights (including copyright and moral rights) in this document are retained by the authors and/or the copyright holders. The express permission of the copyright holder must be obtained for any use of this material other than for purposes permitted by law.

- Users may freely distribute the URL that is used to identify this publication.
- Users may download and/or print one copy of the publication from the University of Birmingham research portal for the purpose of private study or non-commercial research.
- User may use extracts from the document in line with the concept of 'fair dealing' under the Copyright, Designs and Patents Act 1988 (?)
- Users may not further distribute the material nor use it for the purposes of commercial gain.

Where a licence is displayed above, please note the terms and conditions of the licence govern your use of this document.

When citing, please reference the published version.

Take down policy

While the University of Birmingham exercises care and attention in making items available there are rare occasions when an item has been uploaded in error or has been deemed to be commercially or otherwise sensitive.

If you believe that this is the case for this document, please contact UBIRA@lists.bham.ac.uk providing details and we will remove access to the work immediately and investigate.

1 **Dislocation network in additive manufactured steel breaks strength-**
2 **ductility trade-off**

3 Leifeng Liu^{1#}, Qingqing Ding^{2#}, Yuan Zhong¹, Ji Zou³, Jing Wu³, Yu-Lung Chiu³, Jixue Li², Ze
4 Zhang², Qian Yu^{2*}, Zhijian Shen^{1*}

5 1. Department of Materials and Environmental Chemistry, Arrhenius Laboratory, Stockholm University,
6 10691 Stockholm, Sweden

7 2. Department of Materials Science & Engineering, Center of Electron Microscopy and State Key
8 Laboratory of Silicon Materials, Zhejiang University, Hangzhou 310027, China

9 3. School of Metallurgy and Materials, University of Birmingham, B15 2TT, UK

10 # These authors contributed equally to this work

11 * E-mail: yu_qian@zju.edu.cn; zhijian.james.shen@mmk.su.se;

12 **Abstract**

13 Most mechanisms used for strengthening crystalline materials, e.g. introducing crystalline
14 interfaces, lead to the reduction of ductility. An additive manufacturing process – selective
15 laser melting breaks this trade-off by introducing dislocation network, which produces a
16 stainless steel with both significantly enhanced strength and ductility. Systematic electron
17 microscopy characterization reveals that the pre-existing dislocation network, which
18 maintains its configuration during the entire plastic deformation, is an ideal “modulator”
19 that is able to slow down but not entirely block the dislocation motion. It also promotes the
20 formation of high density of nano-twins during the plastic deformation. Meanwhile, notable
21 strain rate hardening also contributes to stabilize the plastic deformation. This finding paves
22 the way for developing high performance metals by tailoring the microstructure through
23 additive manufacturing processes.

24 **Key words:** Additive manufacturing; Selective laser melting; Stainless steel; Mechanical
25 property; Transmission electron microscopy;

26 **1. Introduction**

27 The motion of dislocations governs the plastic deformation hence the mechanical properties
28 of many metals.^{1,2,3} The strength of the metals can be improved by hindering dislocation
29 motion through the designing of microstructure including introducing secondary phases,
30 grain boundaries and other internal interfaces.⁴ Unfortunately most of such strategies that
31 effectively strengthen materials **sacrifice ductility**, resulting in the so called strength-ductility
32 trade-off.⁵ Although a few methods have shown the capability of improving strength while
33 retaining the ductility of materials (for instance by introducing coherent twin boundaries^{2,6},
34 introducing bimodal grain sizes⁷ and by controlling the size, morphology and distribution of

35 secondary phases^{8,9}), making final parts with complex shapes from these methods requires
36 intensive additional machining and may even not be feasible in some cases.

37 Selective laser melting (SLM) is a type of additive manufacturing (AM) processes which is
38 now rapidly changing the ecosystem of manufacturing by enabling the manufacturing of
39 complex components directly from digital files, thus benefiting the customized production
40 and the freedom of designing.¹⁰ During SLM, particle granules are fused directly into 3D
41 components by repetitive scanning of a high energy laser beam over each layer of powder
42 granules, thereby consolidating them via partial or full melting. Another important feature of
43 AM is the ultrafast cooling rate (10^3 - 10^8 K/s). Unlike the other rapid cooling techniques e.g.
44 splat quenching and melt spinning which can produce only metals in low dimensional shapes
45 e.g. metal powder, ribbon and foil, AM can produce metals in 3-dimensional shapes (bulk
46 parts) with extraordinary high cooling rate.¹¹⁻¹⁴ The bulk metal parts show microstructures
47 distinct from those produced by traditional manufacturing routes such as casting and
48 wrought processes.¹⁵⁻²¹ In this study, we show that a dislocation network structure with the
49 accompanying segregation of the alloying elements produced during SLM manufacturing of
50 316L stainless steel (316LSS) leads to unprecedented mechanical properties of a
51 combination of enhanced yield strength and ductility compared to those with the same
52 composition but produced in the other manufacturing processes.²²⁻²⁸ In-situ SEM and TEM
53 study reveals that the dislocation network with the accompanying segregation provides high
54 density of “flexible interfaces” that significantly tunes the dislocation behaviours, resulting in
55 the ameliorated mechanical properties. The results indicate the possibility to directly
56 manufacture products with good combination of strength and ductility while retain the
57 benefits of the process in manufacturing parts with complex or customized geometries.

58 **2. Materials and Methods**

59 **2.1 Sample manufacturing process**

60 As received gas-atomized spherical 316LSS powder with the granular size ranging from 10 to
61 45 μm was purchased from Carpenter powder products AB, Torshälla, Sweden. The
62 standard build was performed by a selective laser melting facility EOSINT M270 (EOS GmbH,
63 Krailing, Germany) equipped with a continuous Nd:YAG fiber laser generator with maximum
64 200 W power output and typically 70 μm diameter laser spot. During the building process, a
65 layer of powder (20 μm in thickness) was laid by a recoating blade on a steel building plate
66 which was preheated to 80 °C. The full laser power of 200 W was used and the laser beam
67 was moving at the speed of 850 mm/s. The laser scanned line by line along the same
68 direction at the same layer and with the line spacing of 100 μm . After the scanning was
69 complete, a new layer of powder was laid and the laser scanned the new layer with the
70 scanning direction rotated by 67°. The sample was built up by repeating this process.

71 To investigate the effect of scanning speed on dislocation cell size, the samples were built up
72 by using standard parameters and the last layer of each sample was scanned by laser with
73 different scanning speed and line spacing (7000 mm/s, 10 μm ; 4250 mm/s, 20 μm ; 283
74 mm/s, 300 μm). The SEM images were taken from the area within the top layers.

75 **2.2 Tensile tests**

76 Tensile test specimens (as-build size $\Phi 8 \times 52$ mm) were prepared by SLM using standard
77 building parameters and machined to cylindrical test specimens (Gage length: 12 mm; gage
78 diameter: 3 mm). All the tensile test bars were built in the same build and with the
79 longitudinal axes along the building direction. Tensile tests were performed according to

80 ASTM E8 with a strain rate of 0.015 min^{-1} up to yield point, and afterward 0.05 min^{-1} till
81 failure. An extensometer was used to measure the elongation. The reported values in this
82 study for tensile properties were the average values of 5 tests.

83 **2.3 Micropillar tests**

84 For the micropillar compression test, two pellets were cut from the same bar built with the
85 longitudinal axis along the building direction. One of them were packed in the stainless steel
86 envelop and heated to $1050 \text{ }^{\circ}\text{C}$ with the ramp rate of $10 \text{ }^{\circ}\text{C}/\text{min}$, kept for 2 hours and
87 followed by water quench. The other one was kept in the as-SLMed state. Two pellets were
88 grinded and polished before micropillar experiment. A commercial Hysitron PI85
89 PicoIndenter installed inside a Tescan Mira-3 scanning electron microscope was used for
90 micropillar compressions. The micropillars with dimensions of about $5 \text{ }\mu\text{m}$, length of about
91 $10 \text{ }\mu\text{m}$ and tapering angles less than 5 degree were fabricated in a FEI Quanta 3D FEG Focus
92 Ion Beam (FIB) by Ga^+ ion beam with the current ranging from 30 nA to 0.1 nA at 30 kV. Both
93 of the two micropillars were fabricated from the grains with the (056) plane parallel to the
94 top surface. The micropillars were then compressed using a flat punch diamond tip with
95 diameter of $20 \text{ }\mu\text{m}$ with constant loading rate of $100 \text{ }\mu\text{N}/\text{s}^{-1}$.

96 **2.4 TEM analysis**

97 TEM specimen were twin-jet electropolished in an alcoholic solution containing 5 vol.%
98 perchloric acid at 30 mA and $-25 \text{ }^{\circ}\text{C}$. Equipped with both bright field and annular dark field
99 detectors, a Cs-corrected FEI 80-200 G² with Super-X operated at 200 kV is employed to
100 analyse the microstructure and elemental distribution of the SLMed 316LSS. The in-situ

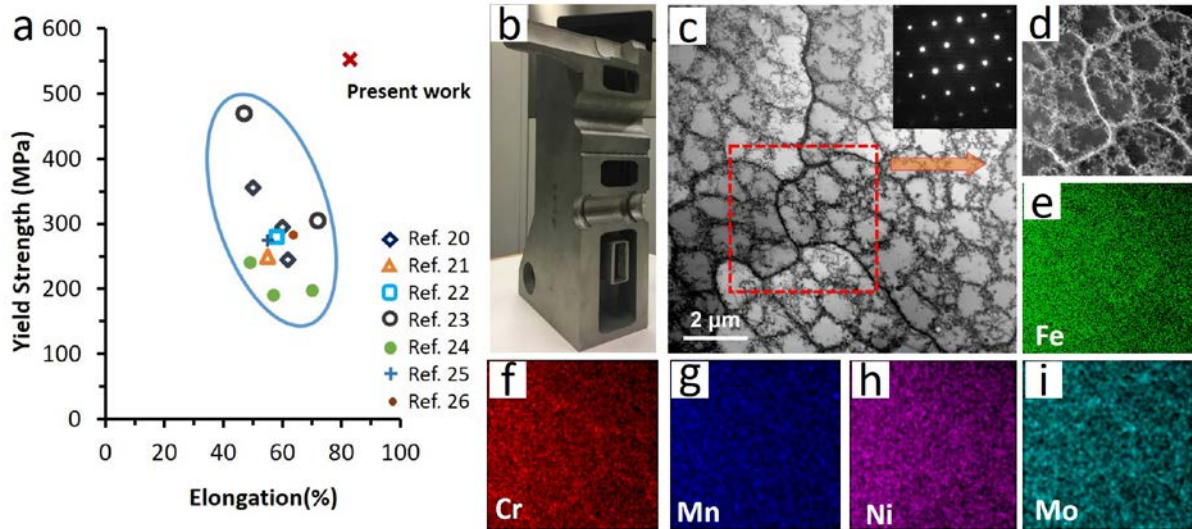
101 tensile tests were achieved by a Gatan model 654 single-tilt straining holder in a FEI Tecnai
102 G2 F20 TEM operated at 200 kV.

103 SEM images were taken on the etched surfaces. Etching was done by submerging the
104 mechanical polished samples into the etching agent (HF:HNO₃:H₂O = 1:4:45) for 60 seconds.

105 **3. Results and discussion**

106 **3.1 Tensile properties of the SLMed 316LSS and TEM characterization of the dislocation** 107 **network structure**

108 Fig. 1b shows a component with the dimensions of 28 cm × 16 cm × 16 cm and a built-in
109 complex internal cooling channel system manufactured by using SLM process from 316LSS
110 powders (particle size: 10µm - 45µm) for the potential application as the first wall panel part
111 in the International Thermonuclear Experimental Reactor (ITER). Tensile tests reveal that the
112 SLMed 316LSS shows notable improvement in both strength and ductility compared to the
113 fully dense 316LSS processed by the other manufacturing methods (Fig. 1a).²²⁻²⁸ The tensile
114 yield strength of 552 ± 4 MPa and elongation to failure of 83.2 ± 0.7 %, was obtained for the
115 SLMed 316LSS (along the building direction). In contrast, the wrought-annealed 316LSS with
116 average grain size of 17.5 µm from Ref.22 shows yield Strength of 244 MPa and failure
117 elongation of 63%.²² A number of previous research on SLMed 316L reported that the
118 process improves the yield strength but reduces or has little effect on ductility.^{11,29,30} The
119 ductility of metals is sensitive to the defects like voids and cracks whose presence largely
120 depends on the process parameters. Only when the defects are suppressed, the contribution
121 from the other factors would be revealed.



122

123

Figure 1. The dislocation network with the accompanying segregation of the alloying elements in

124

SLMed 316LSS. a, The yield strength and ductility data of the SLMed 316LSS and the fully dense

125

316LSS from literature. The elongation to failure was used. **b,** A photo of the ITER first wall penal part

126

manufactured by SLM. **c,** A bright field (BF) STEM image of the dislocation network in the SLMed

127

316LSS with the corresponding selected area electron diffraction (SAED) pattern which shows the

128

single grain signal. **d-i,** An annular dark field (ADF) STEM image and elemental distribution maps of

129

the selected area in **c**.

130

Residual stress can be generated during SLM process, but it was not considered as the main

131

factor affecting the tensile results in this work. Previous studies show that residual stress in

132

SLMed sample can be comparable to the yield strength of the material near the top surface

133

but is much lower in the lower part of the sample.³¹⁻³³ The gage section of the tensile test

134

bar in this study is far below the top surface. Moreover the building plate was preheated to

135

80 °C during process to reduce the residual stress. Thus the residual stress is unlikely to have

136

much effect on the tensile results. The microstructure of the material is then considered as

137

the main reason for the ameliorated mechanical properties. The SLMed 316LSS is composed

138

of mainly columnar grains with the diameters ranging from a few to tens of micrometres and

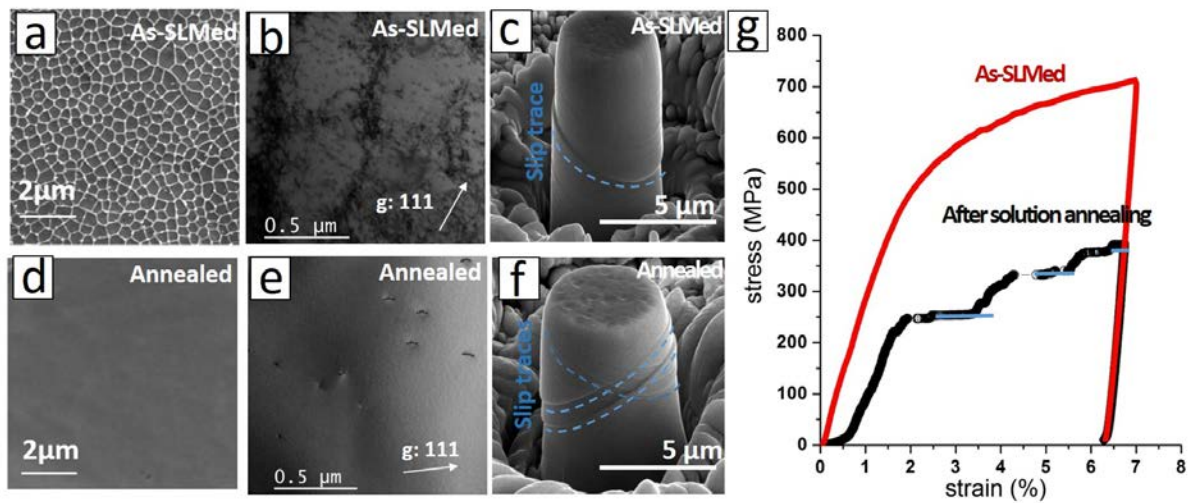
139 lengths up to hundreds of micrometres. TEM analysis reveals a unique dislocation network
140 embedded in individual grains. The dislocation network has been previously found only in 1D
141 or 2D structures (e.g. the welding track or laser treated metal surface^{34,35}), but not in bulk
142 metals produced by any other manufacturing methods. Figure 1c shows the typical
143 dislocation network within a coarse grain, with dislocations concentrated as the wall of
144 columnar cells. SEM analysis shows that the cells have an average diameter of around 500
145 nm and lengths ranging from a few micrometres to a few tens micrometres. The dislocation
146 cells are often aligned with the temperature gradient direction in the solidification process.
147 The elemental maps (Fig. 1e-i) from energy dispersive spectroscopy (EDS) analysis show that
148 the element distribution on the dislocation network is fairly uniform with slight segregation
149 of Cr, Mo and Mn at the walls. Quantitative EDS analysis was performed on five random
150 spots at the dislocation walls and in the other areas, respectively. The results (Table 1) show
151 that Mo, Mn, Cr and Ni content at the dislocation network are all higher than those in the
152 other areas. The formation of dislocation network structure with the accompanying
153 segregation of the alloying elements is due to the cellular growth mode under the high
154 temperature gradient and high growth rate condition.³⁵ Slight orientation differences for the
155 neighbouring cells cause the dense dislocation walls to form when cells grow together into
156 coarse single grains. Meanwhile, the solidification front rejects the alloying elements to the
157 liquid phase leading to higher content of alloying elements at the later solidified region – the
158 cell boundaries.³⁶ Dislocation cells can also form after plastic deformation in a wide range of
159 metals. The flow strength of the deformed metal is inversely linked to the size of such cells.
160 Therefore the dislocation cells in SLMed 316LSS is presumably the main reason of the
161 improved mechanical property.

162 **Table 1.** The content of the elements at the cell wall and inside the cell (wt.%) from EDS analysis.

Element position	Fe	Cr	Ni	Mo	Mn
Cell wall	65.9±1.30	18.5±0.65	11.0±0.16	2.8±0.50	1.74±0.06
Cell inner	69.9±0.11	16.7±0.24	10.3±0.14	1.59±0.11	1.42±0.05

163 **3.2 The strengthening effect of dislocation network confirmed by Micropillar compression**
 164 **tests**

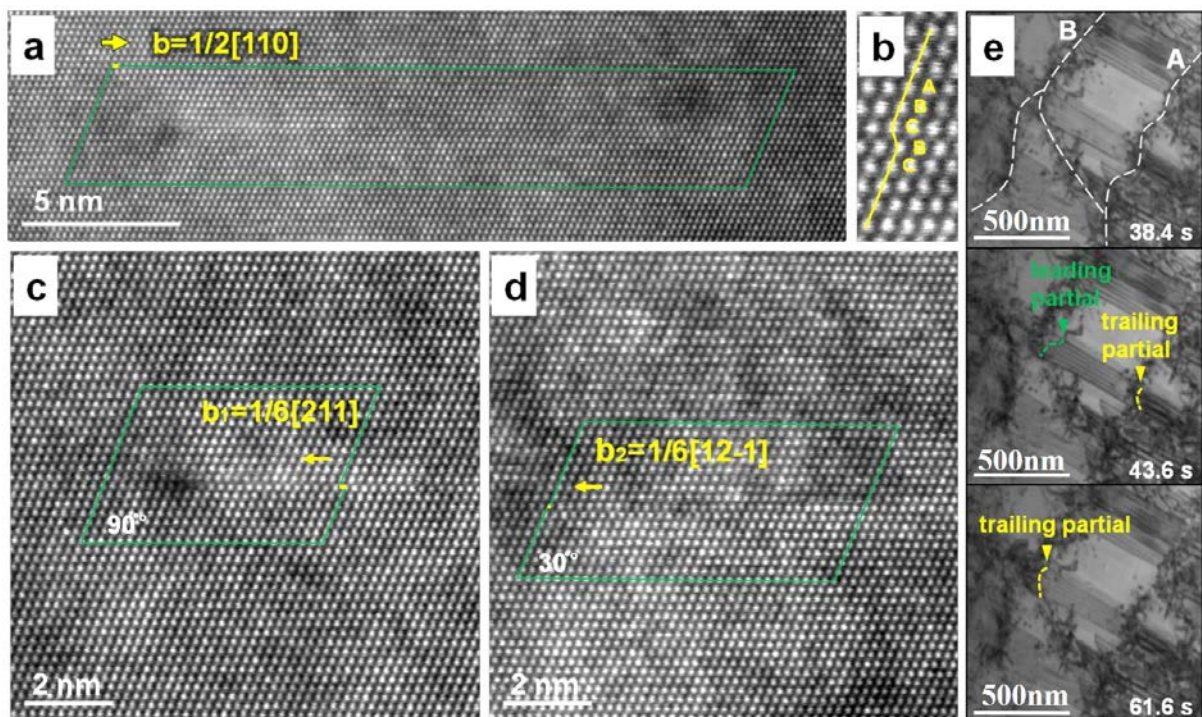
165 To examine the role of this characteristic dislocation network in affecting the mechanical
 166 properties, we performed micropillar compression tests on two samples, viz. the as-SLMed
 167 316LSS whose microstructure was decorated by dislocation network and SLMed-annealed
 168 316LSS which was free of dislocation network after annealing at 1050 °C for 2 hours (Fig. 2a,
 169 b, d, e).



170
 171 **Figure 2. Micropillar compression test result.** a, b, SEM and TEM images of the microstructure of the
 172 as-SLMed 316LSS. c, Compression tested micropillar of the as-SLMed 316LSS. d, e, SEM and TEM
 173 images of the microstructure of the annealed 316LSS. f, Compression tested micropillar of the
 174 annealed 316LSS. g, The engineering stress-strain curves obtained from two micropillars. The as-
 175 SLMed sample shows almost doubled yield strength and much smoother plastic flow behavior than
 176 the annealed sample.

177 Both single crystal micropillar samples were of the same size (5 μm in diameter) before
 178 pressing and were compressed along the [0 5 6] direction. As shown in Fig. 2g, the yield
 179 strength is about 240 MPa for the annealed sample in contrast to 460 MPa for the as-SLMed
 180 sample. The three remarkable plateaus on the stress-strain curve correspond to the three
 181 slip traces on the surface of the annealed micropillar (Fig. 2f), indicating that catastrophic
 182 shear-off happened quite often due to the escape of large number of dislocations from the
 183 intersections of the same slip planes and the surface. In contrast, the as-SLMed pillar had
 184 smoother plastic flow behaviour. It indicates that with the dislocation network, the as-
 185 SLMed pillar had much better ability of dislocation storage where dislocations found
 186 significant difficulty during glide before they eventually slipped out from the surface
 187 therefore displayed both higher strength and better plastic stability.

188 **3.3 Effects of the dislocation network on dislocation motion and twin formation revealed**
 189 **by in-situ TEM analysis**

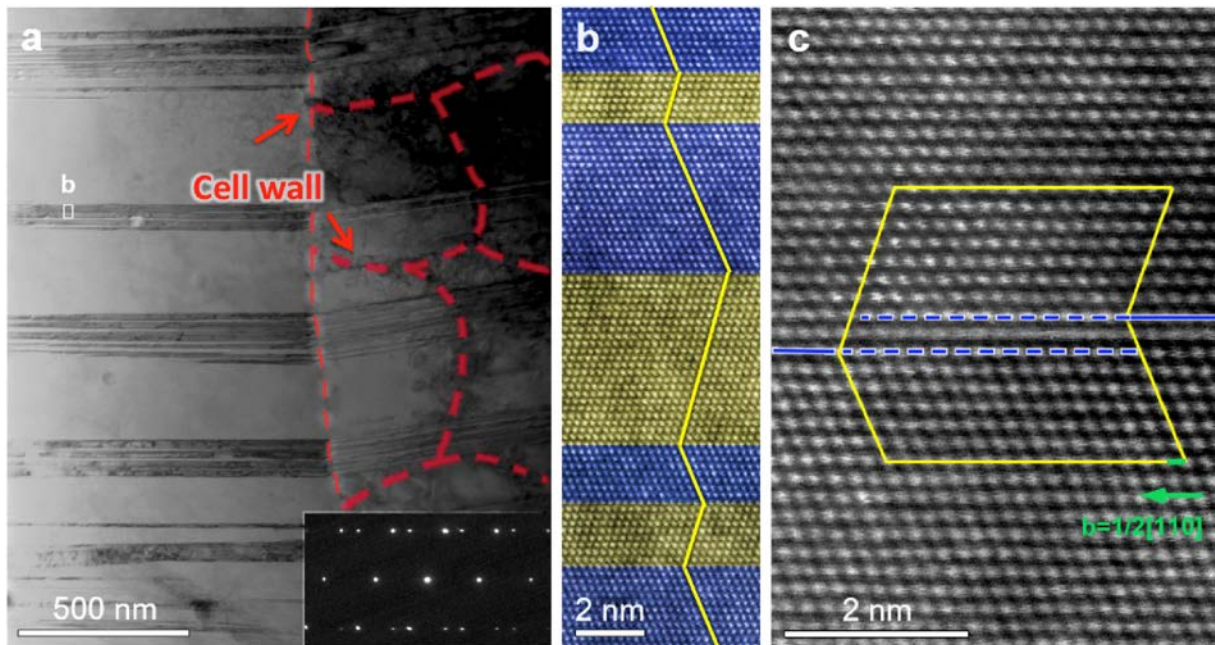


190

191 **Figure 3. Dislocations in SLMed 316LSS.** **a**, A high-angle annular dark field (HAADF)-STEM image of a
192 partial dislocation pair within a cell in the as-SLMed sample. **b-d**, High resolution annular dark
193 field (ADF)-STEM images showing the stacking fault, trailing partial dislocation and leading partial
194 dislocation in **(a)**. **e**, Screenshots from the Video 1 showing interaction between partial dislocations
195 and dislocation cell walls.

196 The details of the dynamic motion and interaction of dislocations within such dislocation
197 network were further investigated by performing in-situ TEM mechanical testing at room
198 temperature by using a Gatan in-situ straining holder. The major carrier for plastic
199 deformation was partial dislocations, whose motion was significantly but not fully impeded
200 by the dislocation network. Dislocations widely dissociated into Shockley partials with jerky
201 motion when they were temporarily trapped by the dislocation walls and would move
202 forward again with the increase of applied stress (Video 1). For instance, as shown in Fig. 3a-
203 d, the partial dislocations within a cell in the as-SLMed sample have Burgers vector $1/6[211]$
204 and $1/6[12-1]$, respectively. The dislocations in the cell walls are also mostly dissociated
205 partial dislocations with Burgers vector $1/6\langle 112 \rangle$. Figure 3e shows the dynamic evolution of
206 stacking fault, which corresponds to the motion of partial dislocation pairs through the
207 dislocation cells. When the external stress was high enough, a leading partial was emitted
208 from a cell wall "A" and stopped at the cell wall "B" against it. At this moment, the trailing
209 partial was still trapped by the cell wall "A". As the applied stress increased gradually, the
210 leading partial overcame the impediment of wall "B" and glided into the neighbouring cell.
211 The trailing partial glided to wall "B" as well. Clearly the motion of dislocations in SLMed
212 316LSS was hindered but not fully stopped by these cell walls. Slip transferred across the
213 cells with increasing strain; therefore the strength was enhanced without sacrificing the
214 ductility. This is a scenario similar to the coherent twin boundaries reported before.² Besides

215 the impediment effect, the complex dislocation network with mostly dissociated partial
216 dislocations might also have supplied sites for nucleation of dislocation loops, with which the
217 dislocation interactions became even more prolific and complicated.



218

219 **Figure 4. STEM micrographs of the SLMed 316LSS after deformation.** **a**, High density of nano-
220 twins in a BF-STEM image. The inset is the selected area electron diffraction pattern obtained from
221 the left side of the sample in **(a)**. **b**, **c**, High resolution (HR)-STEM micrographs showing the atomic
222 structures of the bunched nano-twins and twin boundary with a step. The twin and matrix are
223 colored into blue and yellow, respectively.

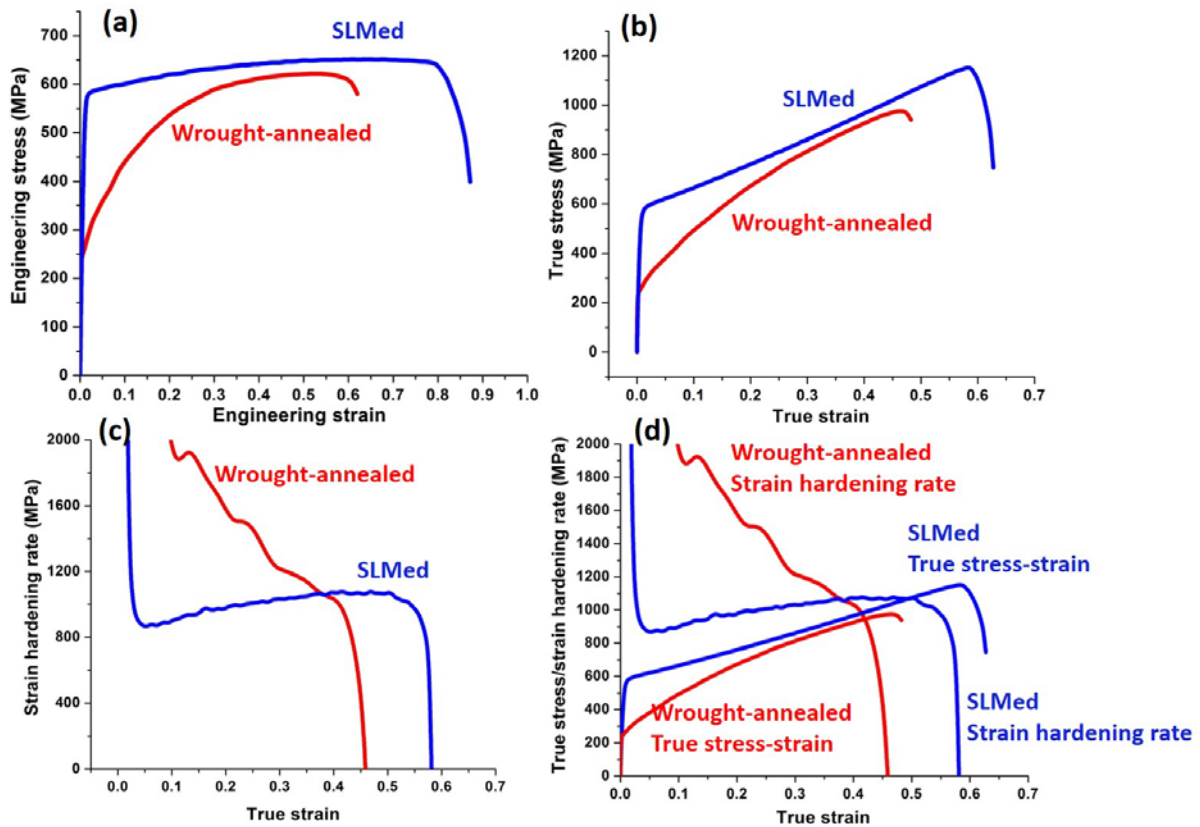
224 Meanwhile, the cell walls could also trap partial dislocations so that some of the paired
225 dislocations lost their partners. Consequently deformation twinning formed as the same
226 type of partial dislocations glided on the adjacent planes. Figure 4a shows nano-twins
227 formed after deformation. The dislocation network was found in the whole visible region;
228 however, due to the slight orientation difference the network on the left side was less visible
229 under this imaging condition. The slim nano-twins oriented along the same direction and
230 usually propagated through several cells. It was also observed that the nano-twins were

231 bunched and initiated from the cell walls and not necessarily from the grain boundaries.
232 Figure 4b shows a HR-STEM image of the nano-twin structure; the thickness of twins ranged
233 from 2 nm to 6 nm in general. However as shown in Fig. 4c, the stable twin can be as thin as
234 two atomic layers, which supports the layer by layer growth mechanism of twins in this case
235 and it experimentally confirms the theoretical simulation which proposed that the minimum
236 thickness of a stable twin in FCC structure is 2 atomic layers.³⁴ Those nano-twins should have
237 significant influence on dislocation motion, resulting in stable plastic deformation by strain
238 hardening through the dynamic Hall-Petch effect similar to that in nano-twined copper and
239 TWIP steels.^{38, 39}

240 **3.4 The mechanism of simultaneously improvements of strength and ductility**

241 Combining the multiscale mechanical properties-structure characterizations and in-situ TEM
242 testing, it is confirmed that the pre-existing dislocation network structure has significant
243 contribution to the high strength and ductility of as-SLMed 316LSS. Firstly the pre-existing
244 dislocation network impedes dislocation motion and thus increases dislocation storage
245 contributing as the main mechanism to the high yield strength. Meanwhile, the segregated
246 alloying elements at the cell walls provide an extra solid solution strengthening effect.
247 Secondly, with the increase of stress, the impeded dislocations are allowed to transmit
248 through the dislocation walls; meanwhile the pinning effect from the segregated atoms
249 effectively stabilizes the dislocation network to maintain its size during the entire plastic
250 deformation, enabling the stable plastic flow. In addition, the misorientation between cells
251 can also contribute to the stability of the dislocation network as well as provides dislocation
252 sources for the continuous plastic flow. Dislocation cells can also form in a wide range of
253 metals after moderate to large strain. In contrast, such dislocation cells strengthen deformed

254 metals but reduce the tensile elongation. A major difference from the cells formed in SLM is
 255 that the wall of such dislocation cells is mobile and the cells shrink as the increase of the
 256 stress. The good stability of pre-existing dislocation network structure even at ultra-high
 257 stress level in our as-SLMed 316LSS is crucial for the enhancement of ductility.

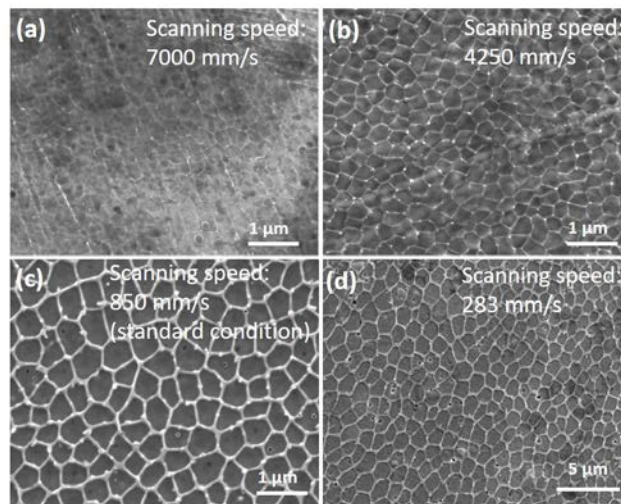


258

259 **Figure 5. Tensile properties of the SLMed 316LSS from the present work and the wrought-annealed**
 260 **316LSS with average grain size of 17.5 μm from Ref. 22.** a, Engineering tensile stress-strain curves. b,
 261 True stress-strain curves. c, Strain hardening rate curves. d, Comparison of the strain hardening rate
 262 and true stress of both SLMed and wrought-annealed 316LSS. Bar specimens with gage diameter and
 263 length of 3 mm and 12 mm were used for tensile test of SLMed samples. Plate specimens with gage
 264 dimensions of 12.5 \times 57 \times 0.75 mm was used in Ref. 22 for the tensile test of wrought-annealed
 265 samples.

266 In general the increase of ductility is achieved by delaying the onset of necking. The necking
267 caused by plastic instability takes place when the Hart criterion is satisfied ($\frac{d\sigma}{d\varepsilon} + m \cdot \sigma \leq \sigma$,
268 where σ is the true stress, ε is the true strain and m is the strain rate sensitivity). So both the
269 strain hardening ($\frac{d\sigma}{d\varepsilon}$) and strain rate hardening ($m \cdot \sigma$) contribute to the delay of necking.³⁷
270 In wrought-annealed 316LSS, the contribution from strain rate hardening is not significant
271 due to a negligible m value at the latter stage of plastic deformation.²⁸ In contrast, SLMed
272 316LSS shows notable elongation after the flow stress outweighs the strain hardening rate,
273 which is presumably from the contribution of strain rate hardening (Fig. 5d). Similar to the
274 ultrafine and nanocrystalline Ni,⁴¹ the concentrated dislocations in dislocation walls lead to a
275 small activation volume and hence a high m value. Besides nano-twins formed during
276 deformation can also cause the increase of m value. On the other hand, the evolution of
277 strain hardening rate also plays an important role for the high tensile elongation of SLMed
278 316LSS. The strain hardening rate of SLMed 316LSS starts at a low value but maintains stable
279 and even gradually increases during entire plastic deformation till the failure. While the
280 wrought-annealed 316LSS shows initially high strain hardening rate but with substantial
281 decrease afterward (Fig. 5c). The difference in the strain hardening rate is highly related to
282 the distinct microstructural evolution processes in the two 316L stainless steels due to the
283 different stability of the dislocation cellular structure. In SLMed 316L, the pre-existing
284 dislocation network structure formed during manufacturing is pinned by the elements
285 segregation and the misorientation across the cell walls. The characteristic size of the
286 dislocation network structure is retained even at the late stage of the plastic deformation
287 when high flow stress is reached. The misorientation across the cell walls can also act as
288 dislocation source. These enable continuous dislocation motion, nanotwins formation and

289 thus the stable plastic flow during the entire plastic deformation. Meanwhile the formation
290 of nano-twins promoted by the dislocation network also contributes to the strain hardening
291 through dynamic Hall-Petch effect to delay the necking. On the contrary, in wrought-
292 annealed 316LSS, dislocation network structure forms during plastic deformation, which
293 contributes to strain hardening rate in the beginning. However, the cells later shrink to small
294 sizes and the dynamic recovery at cell boundaries leads to the decrease of work hardening
295 rate.⁴²⁻⁴⁴



296

297 **Figure 6. Different scanning speeds result in different sizes of the dislocation cells. a-d**, SEM images
298 from the etched surfaces of the samples built with laser scanning speed of (a) 7000 mm/s; (b), 4250
299 mm/s; (c) 850 mm/s and (d) 283 mm/s.

300 Importantly the cell size and morphology of the dislocation network which are sensitive to
301 the cooling rate and temperature gradient are also tunable by changing the cooling speed.
302 As shown in Fig. 6, the cell size of the dislocation network is effectively adjusted to be
303 around 200 nm, 250 nm, 500 nm and 1 μm, respectively, by using different scanning speed
304 (7000, 4250, 850 and 283 mm/s) to tune the cooling speed. It indicates that the mechanical

305 properties of SLMed alloys can be designed purposefully based on its controllable
306 microstructure-properties relationship.

307 **4. Conclusions**

308 To sum, besides the ability to produce complex shaped parts, the AM processes also provide
309 ultra-fast cooling rate during solidification which results in unique microstructure that
310 consequently leads to outstanding mechanical properties in bulk metal parts that is not
311 possible to be achieved by any other so far established manufacturing method. A systematic
312 SEM and TEM work reveals that the dislocation network with the accompanying segregation
313 of alloying elements acts as stable and “soft” barriers that hinder dislocation motion for
314 strength but meanwhile guarantee continuous plastic flow by allowing dislocations from
315 transmitting. This strategy to improve both the strength and ductility by introducing a
316 dislocation network may also be applied to other alloys with low stacking fault energy. In
317 addition, the mechanical properties can potentially be designed purposefully since its
318 microstructure is directly tuneable by scanning parameters. This work paves the way for
319 developing high performance metals with desired mechanical properties by in situ tailoring
320 the microstructure during the manufacturing process thus further boosting the AM as a
321 disruptive technology to reshape the manufacturing.

322 **Acknowledgements**

323 Thanks to Dr. Mirva Erikson and Jon Olsen for the proof reading.

324 This work is financially supported by Fusion for Energy (F4E) [F4E-GRT-516]; Chinese 1000-
325 Youth-Talent Plan [Qian Yu]; 111 project [No.B16042]; National Natural Science Foundation

326 of China [51671168]; and the State Key Program for Basic Research in China [No.
327 2015CB65930].

328 **Reference**

- 329 1. W.F. Smith, & J. Hashemi, Foundations of materials science and engineering, McGraw-
330 Hill, New York, 2005.
- 331 2. D. Hull, D.J. Bacon, Introduction to Dislocations, fourth ed., Elsevier, Amsterdam,
332 2001.
- 333 3. Q. Yu, et al. Origin of dramatic oxygen solute strengthening effect in titanium, Science
334 347 (2015) 635–639.
- 335 4. K. Lu, L. Lu, S. Suresh, Strengthening materials by engineering coherent internal
336 boundaries at the nanoscale, Science 324 (2009) 349–652.
- 337 5. K. Kumar, H. Van Swygenhoven, S. Suresh, Mechanical behavior of nanocrystalline
338 metals and alloys, Acta Mater. 51 (2003) 5743–5774.
- 339 6. L. Lu, Y. Shen, X. Chen, L. Qian, K. Lu, Ultrahigh strength and high electrical
340 conductivity in copper, Science 304 (2004) 422–426.
- 341 7. Y. Wang, M. Chen, F. Zhou, E. Ma, High tensile ductility in a nanostructured metal,
342 Nature 419 (2002) 912–915.
- 343 8. X. Wu, et al. Heterogeneous lamella structure unites ultrafine-grain strength with
344 coarse-grain ductility, Proc. Natl. Acad. Sci. 112 (2015) 14501–14505.
- 345 9. S. H. Kim, H. Kim, N.J. Kim, Brittle intermetallic compound makes ultrastrong low-
346 density steel with large ductility, Nature 518 (2015) 77–79.
- 347 10. B. Berman, 3-D printing: The new industrial revolution, Bus. Horiz. 55 (2012) 155–162.
- 348 11. D. Herzog, V. Seyda, E. Wycisk, C. Emmelmann, Additive manufacturing of metals,
349 Acta Mater. 117 (2016) 371–392.

- 350 12. S.A. Khairallah, A.T. Anderson, A. Rubenchik, W. King, Laser powder-bed fusion
351 additive manufacturing: Physics of complex melt flow and formation mechanisms of
352 pores, spatter, and denudation zones, *Acta Mater.* 108 (2016) 36–45.
- 353 13. E. W. Collings, A. J. Markworth, J. K. McCoy, J. H. Saunders, Splat-quench solidification of
354 freely falling liquid-metal drops by impact on a planar substrate, *J. Mater. Sci.* 25
355 (1990) 3677-3682.
- 356 14. D. Pavuna, Production of metallic glass ribbons by the chill-block melt-spinning
357 technique in stabilized laboratory conditions, *J. Mater. Sci.* 16 (1981) 2419-2433.
- 358 15. X.P. Li, et al. A selective laser melting and solution heat treatment refined Al-12Si alloy
359 with a controllable ultrafine eutectic microstructure and 25% tensile ductility, *Acta*
360 *Mater.* 95 (2015) 74–82.
- 361 16. B. Qian, et al. Defects-tolerant Co-Cr-Mo dental alloys prepared by selective laser
362 melting, *Dent. Mater.* 31 (2015) 1435–1444.
- 363 17. G. A. Ravi, C. Qiu, M.M. Attallah, Microstructural control in a Ti-based alloy by
364 changing laser processing mode and power during direct laser deposition, *Mater. Lett.*
365 179 (2016) 104–108.
- 366 18. L. Thijs, F. Verhaeghe, T. Craeghs, J.V. Humbeeck, J.P. Kruth, A study of the
367 microstructural evolution during selective laser melting of Ti–6Al–4V, *Acta Mater.* 58
368 (2010) 3303–3312.
- 369 19. B. Vrancken, L. Thijs, J.P. Kruth, J.V. Humbeeck, Microstructure and mechanical
370 properties of a novel β titanium metallic composite by selective laser melting, *Acta*
371 *Mater.* 68 (2014) 150–158.
- 372 20. J. Wu, X.Q. Wang, W. Wang, M.M. Attallah, M.H. Loretto, Microstructure and strength
373 of selectively laser melted AlSi10Mg, *Acta Mater.* 117 (2016) 311–320.
- 374 21. Y. Zhong, L. Liu, S. Wikman, D. Cui, Z. Shen, Intragranular cellular segregation network
375 structure strengthening 316L stainless steel prepared by selective laser melting. *J.*
376 *Nucl. Mater.* 470 (2016) 170–178.

- 377 22. W.A. Poling, Grain Size Effects in Micro-Tensile Testing of Austenitic Stainless Steel,
378 MS thesis, Colorado School of Mines, 2012.
- 379 23. X.H. Chen, J. Lu, L. Lu, K. Lu, Tensile properties of a nanocrystalline 316L austenitic
380 stainless steel, *Scr. Mater.* 52 (2005) 1039–1044.
- 381 24. S. Maloy, et al. The mechanical properties of 316L/304L stainless steels, Alloy 718 and
382 Mod 9Cr–1Mo after irradiation in a spallation environment, *J. Nucl. Mater.* 296 (2001)
383 119–128.
- 384 25. F.K. Yan, G.Z. Liu, N.R. Tao, K. Lu, Strength and ductility of 316L austenitic stainless
385 steel strengthened by nano-scale twin bundles, *Acta Mater.* 60 (2012) 1059–1071.
- 386 26. A.M. Brass, J. Chêne, Hydrogen uptake in 316L stainless steel: Consequences on the
387 tensile properties, *Corros. Sci.* 48 (2006) 3222–3242.
- 388 27. V. Ganesan, M.D. Mathew, K.B. Sankara Rao, Influence of nitrogen on tensile
389 properties of 316LN SS, *Mater. Sci. Technol.* 25 (2009) 614–618.
- 390 28. G.S. Langdon, G.K. Schleyer, Unusual strain rate sensitive behaviour of AISI 316L
391 austenitic stainless steel, *J. Strain Analysis* 39 (2015) 71-86.
- 392 29. H.D. Carlton, A. Haboub, G.F. Gallegos, D.Y. Parkinson, A.A. MacDowell, Damage
393 evolution and failure mechanisms in additively manufactured stainless steel, *Mater.*
394 *Sci. Eng. A* 651 (2016) 406-414.
- 395 30. A. Riemer, S. Leuders, M. Thöne, H.A. Richard, T. Tröster, T. Niendorf, On the fatigue
396 crack growth behavior in 316L stainless steel manufactured by selective laser melting,
397 *Eng. Fract. Mech.* 120 (2014) 15-25.
- 398 31. X. Song, et al, Residual stresses and microstructure in Powder Bed Direct Laser
399 Deposition (PB DLD) samples, *Int. J. Mater. Form.* 8 (2015) 245–254.
- 400 32. M. Shiomi, K. Osakada, K. Nakamura, T. Yamashita, F. Abe, Residual Stress within Metallic
401 Model Made by Selective Laser Melting Process, *CIRP Annals*, 53 (2004) 195-198.
- 402 33. I.A. Roberts, Investigation of residual stresses in the laser melting of metal powders in

- 403 additive layer manufacturing, PhD Thesis, University of Wolverhampton, 2012.
- 404 34. V. Shankar, T.P. Gill, S. Mannan, S. Sundaresan, Effect of nitrogen addition on
405 microstructure and fusion zone cracking in type 316L stainless steel weld metals,
406 Mater. Sci. Eng. A 343 (2003) 170–181.
- 407 35. S. Kou, Welding metallurgy, John Wiley & Sons, New Jersey, 2003.
- 408 36. E. Kannatey-Asibu, Principles of laser materials processing, John Wiley & Sons, New
409 Jersey, 2009.
- 410 37. S. Ogata, J. Li, S. Yip, Energy landscape of deformation twinning in bcc and fcc metals,
411 Phys. Rev. B 71 (2005) 224102.
- 412 38. L. Lu, X. Chen, X. Huang, K. Lu, Revealing the maximum strength in nanotwinned
413 copper, Science 323 (2009) 607–610.
- 414 39. Z. Li, K.G. Pradeep, Y. Deng, D. Raabe, C.C. Tasan, Metastable high-entropy dual-phase
415 alloys overcome the strength–ductility trade-off. Nature 534 (2016) 227-230.
- 416 40. E.W. Hart, Theory of the tensile test, Acta Metallurgica 15 (1967) 351-355.
- 417 41. Y.M. Wang, A.V. Hamza, E. Ma, Temperature-dependent strain rate sensitivity and
418 activation volume of nanocrystalline, Ni. Acta Mater. 54 (2006) 2715-2726.
- 419 42. M. Nabil Bassim, R.J. Klassen, Variation in dislocation cell size with local strain in a low
420 alloy steel, Mater. Sci. Eng. 81 (1986) 163–167.
- 421 43. R.N. Gardner, T.C. Pollock, H.G.F. Wilsdorf, Crack initiation at dislocation cell
422 boundaries in the ductile fracture of metals, Mater. Sci. Eng. 29 (1977) 169 – 174.
- 423 44. X. Feaugas, On the origin of the tensile flow stress in the stainless steel AISI 316L at
424 300 K: back stress and effective stress, Acta Mater. 47 (1999) 3617–3632.

425 **Author Contributions**

426 Z.S., Q.Y. and L.L. designed the research; Y.Z. and L.L. fabricated the samples; Q.D. performed
427 the in-situ TEM work and the data analysis; J.Z. and J.W. carried out the micropillar
428 compression tests; L.L., Q.D., Q.Y., L.C and Z.S. wrote the manuscript; all the authors
429 contributed to the discussions and commented the manuscript.

430 **Competing Financial Interests statement**

431 The authors declare no competing financial interests.